Energy & Environmental Science

Accepted Manuscript

ROYAL SOCIETY OF CHEMISTRY

www.rsc.org/ees

Cite this: DOI: 10.1039/c0xx00000x

www.rsc.org/xxxxxx

ARTICLE TYPE

Colossal pseudocapacitance in a high functionality - high surface area carbon anode doubles the energy of an asymmetric supercapacitor

Zhi Li,[ab] Zhanwei Xu, [ab] Huanlei Wang*[ab] Jia Ding, [ab] Beniamin Zahiri, [ab] Chris M. B. Holt, [ab] Xuehai Tan, [ab] and David Mitlin*[ab]

Received (in XXX, XXX) Xth XXXXXXXXX 20XX, Accepted Xth XXXXXXXXX 20XX
DOI: 10.1039/b000000x

Here we demonstrate a facile template-free synthesis route to create macroscopically monolithic carbons that are both highly nitrogen rich (4.1-7.6 wt.%) and highly microporous (SA up to 1405 m^2 g^{-1}, 88vol% micropores). While such materials, which are derived from common chicken egg whites, are expected to be useful in a variety of applications, they are extremely promising for electrochemical capacitors based on aqueous electrolytes. The Highly Functionalized Activated Carbons (HFACs) demonstrate a specific capacitance > 550 F g^{-1} at 0.25A g^{-1} and > 350 F g^{-1} at 10 A g^{-1} in their optimized state. These are among the highest values reported in literature for carbon-based electrodes, including for systems such as templated carbons and doped graphene. We show that HFACs serve as ideal negative electrodes in asymmetric supercapacitors, where historically the specific capacitance of the oxide-based positive electrode was mismatched to the much lower specific capacitance of the opposing AC. An asymmetric cell employing HFACs demonstrates a 2X higher specific energy and a 4X higher volumetric energy density as compared to the one employing a high surface area commercial AC. With 3.5 mg cm^{-2} of HFAC opposing 5.0 mg cm^{-2} of $NiCo_2O_4$/graphene, specific energies (active mass normalized) of 48 Wh kg^{-1} at 230 W kg^{-1} and 28 Wh kg^{-1} at 1900 W kg^{-1} are achieved. The asymmetric cell performance is among the best in literature for hybrid aqueous systems, and actually rivals cells operating with a much wider voltage window in organic electrolytes.

Introduction

Electrochemical capacitors (supercapacitors) are a class of energy-storage devices that are able to operate at a much higher power density than conventional batteries, though at the expense of a considerably lower energy density. In the last decade, research in supercapacitor materials and electrolytes leading to improved energy storage capacities has been motivated by numerous existing and potential applications. One emerging application of supercapacitors is in electric/hybrid heavy and consumer automotive vehicles, which can employ a high power device to supply a surge during startup (heavy) and to convert kinetic energy associated with vehicle braking into useful electricity (consumer automotive). [1, 2] Supercapacitors are categorized into electric double-layer capacitors (EDLCs) that store energy based on the accumulation of charge in the double layer formed at the surface of inert electrodes, and pseudocapacitors that primarily derive their energy storage capacity from reversible faradaic reactions that occur on the active material's surface. [3] In the latter case there is still an EDLC contribution to the overall capacitance, though is usually of secondary importance due to a lower surface area of pseudocapacitive materials.

In aqueous electrolytes, the vast majority of EDLCs are based on high surface area microporous activated carbons and related materials, with specific capacitance in 150-200 F g^{-1} range and lower (based on the weight of the active material). [4] Conversely, pseudocapacitors, which are primarily based on nanostructured metal oxides, possess capacitances as high as 1,000-2,000 F g^{-1}. However oxide-based pseudocapacitors possess a narrow useful voltage window where they are stable from dissolution. [5, 6]. Therefore the really useful application of oxide-based electrodes is in asymmetric devices composed of metal oxides as positive electrodes opposing some form of a high surface area carbon (*e.g.* activated carbon, CNTs or graphene) as a negative electrode. Such systems have demonstrated substantial advantages over symmetric configurations, including a wider operating voltage window (~ 1.5 V *vs.* < 1.2 V) due to kinetic suppression of oxygen evolution on the oxide surface.[7, 8] Significant progress has been achieved in enhancing the electrochemical performance of the positive electrodes by introducing a secondary nanodispersed carbon phase that acts as a highly electrically conductive skeleton, reducing the IR losses.[6, 9, 10, 11]

The capacitance of an electrochemical cell is decided by both electrodes, as defined by the formula: $1/C_{cell}=1/C_{+} + 1/C_{-}$, where C_{cell} is the cell capacitance, C_{+} and C_{-} are the capacitances of the positive and the negative electrodes. Since the specific capacitance of metal oxides is usually much higher than that of the opposing carbon, the cell capacitance (and therefore cell

energy) is limited by C-. Therefore, negative electrodes with improved capacitances are highly desirable. Such electrodes are primarily based on various advanced carbon architectures, including activated carbon nanofibers, carbon nanotubes, reduced graphene oxide, graphite foams, etc. [2, 7, 10-12, 13-20]

Carbon materials with highest capacitances in aqueous electrolytes are those with both high surface areas and high surface heteroatom content (such as O, N and B), derived from precursors rich in those elements. [21-24] These materials can typically deliver a capacitance as high as 250-400 F g^{-1} due to the pseudocapacitive contribution from the redox process of the heteroatom surface functionalities.[20, 25, 26-28] The N-doped carbons also possess improved electrical conductivity compared to their pure counterparts. [29] Recent research on graphene oxide and N-doped graphene demonstrated that these functionalities may have much more impact on the capacitive performance than was initially realized. [30] A extreme example is the recently reported poly(o-phenylenediamine)-derived carbon materials with 23% N and 16% O. The material, which has the morphology of crumpled nanosheets, exhibits a specific capacitance over 600 F g^{-1} at a sweep rate of 1 mV/sec, degrading to ~ 75 F g^{-1} at 100 mV/S. To obtain the capacitance values the authors employed a voltage window (0.7 V) that is unusually narrow for a carbon electrode, making a direct comparison to other literature difficult. [31] Alternatively, N and O-doped carbons may be obtained by pyrolyzing biomass that is naturally rich in these elements. For example, functionalized carbons with very promising electrochemical characteristics have been recently obtained from gelatin,[32] bacteria,[33] dead leaves[34] and human hairs.[35]

One key outstanding issue is how to combine this high content of heteroatom functionalities with an active surface area that is comparable to that of commercial dopant-free activated carbons (*e.g.* > 1000 m^2 g^{-1}). This would further boost the specific capacitance of the negative electrode to be closer to that of the opposing oxide. Achieving this in practice, however, presents a conundrum: Surface modification of "pure" high surface area carbons works initially, but results in relatively rapid performance degradation with cycling due to the dissolution of the electroactive surface moieties. Conversely, further activation of heteroatom rich carbons requires such high temperatures to achieve the target surface area, that the functionalities are inadvertently eliminated in the process. [26, 28, 32] While hard templating techniques have been employed to convert N-rich precursors to relatively high surface area (400-800 m^2 g^{-1}) carbons with the surface heteroatoms still intact,[36, 37] the intrinsic complexity of such synthesis methods may preclude their wide-scale utilization. Ideally one would rather employ a simple template-free process to achieve this dual target. We here demonstrate unique success in creating a facile synthesis methodology that converts an agricultural-derived N-rich precursor (chicken egg whites) into supercapacitor electrode carbons that possess high surface area and high functionality, together on a scale that has not been previously achieved. This synergy imparts an exquisite electrochemical performance to these materials, making them ideally suited as negative electrodes in asymmetric cells.

Experimental Section

Materials

The eggs used in the experiments were produced at Sparks egg farm in Calgary. All reagents were purchased from Aldrich, unless otherwise specified and were used without further purification.

Synthesis of Low Temperature Activated Egg White

Egg white (50 mL, roughly the amount from two eggs) was first diluted with 200 mL water to form a transparent protein solution. Ethanol (250 mL) was poured into the protein solution to precipitate the proteins. The precipitated egg white was then filtered out and pyrolyzed in a tubular furnace (650 ^oC for 2 hours, heating rate: 5 ^oC min^{-1}) under argon atmosphere. The pyrolyzed egg white (named as HFC), mixed with different amount of KOH, was further activated at 550 ^oC for 2 hours under argon atmosphere and named as HFAC-*n*, where *n* indicates the KOH/HFC mass ratio. The obtained fine carbon powder was washed with HCl (6M) overnight to remove the impurities and rinsed 3 times with DI water before use.

Synthesis of $NiCo_2O_4$/graphene as Positive Electrode

The synthesis of $NiCo_2O_4$/graphene followed the procedure that we reported previously.[13] In brief, a mixture of acid-treated graphene (0.1 g, dispersed in 100 mL of deionized water), hexadecyltrimethylammonium bromide (CTAB, 1 g), urea, nickel nitrate hexahydrate, and cobalt chloride hexahydrate (the molar ratio of Ni^{2+}: Co^{2+}: urea was 1:2:45) was sonicated for 1h and then transferred in a sealed container and held for 100 ^oC under stirring for 6 h. The resulting powder was collected, washed with deionized water and calcined at 350 ^oC for 3 h in air.

Electrochemical Characteristics

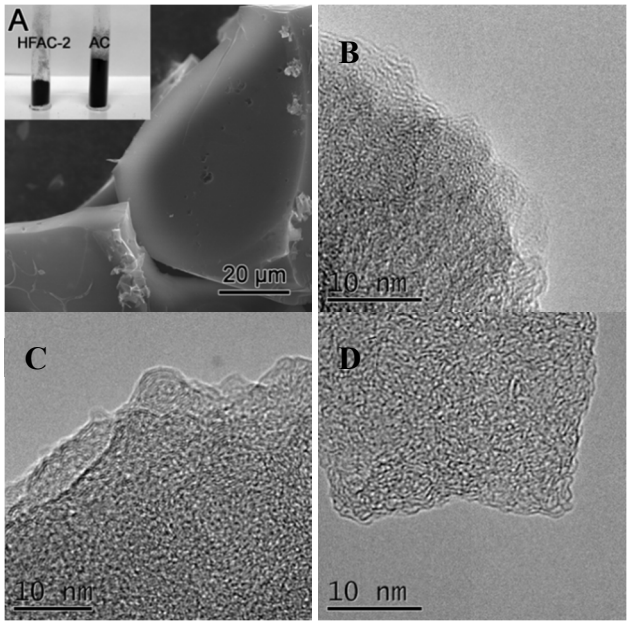

Fig. 1(A) SEM image of HFAC-2 with the inset showing the volume difference in comparison with baseline AC with the same weight; (B)-(E) high resolution TEM micrographs of HFAC-1, HFAC-2 and HFAC-3.

The electrochemical performance of HFAC was investigated employing both a 3 electrode configuration, and a 2 electrode cell

asymmetric (hybrid) cell with $NiCo_2O_4$/graphene as a positive electrode. For testing in a 3 electrode setup, a slurry of 85% active materials, 10% carbon black (Super-P) and 5 % PVDF (binder) in N-methylpyrrolidone (NMP) solvent is coated onto a glassy carbon disc and then dried at 110 °C overnight in a vacuum oven. The obtained working electrode possessed a mass loading of around 1mg cm^{-2}. The working electrode was tested with Pt wire as counter electrode, $Hg/HgSO_4$ (saturated K_2SO_4) and Hg/HgO (1M NaOH) as reference electrodes in 1M H_2SO_4 and 1M KOH, respectively. The specific capacitance is calculated as $It/m\Delta E$, where I is the change/discharge current, t is the discharging time, m is the mass of electrode materials and ΔE stands for the potential window. For the test in asymmetric cell, active materials (75%) were first mechanically mixed with Super-P (15%) and PVDF (10%) with small amount of NMP to obtain a semi-solid paste. Then the thick paste was screen printed onto 1 cm^2 nickel foam (current collector), dried at 110 °C overnight and physically sandwiched between two pieces of nickel foam under a pressure of 100 MPa for additional mechanical support. The positive electrode ($NiCo_2O_4$/graphene) and negative electrode (HFAC-2 or AC) were placed face-to-face and tested in 1M KOH. The mass loading of the active materials ranged from 3.5-10.1 mg cm^{-2}. Cyclic voltammetry, galvanostatic charge-discharge cycling, and impedance analysis are performed using a Solatron 1470E Multichannel Potentiostat/CellTest System.

Chemical Analysis and Textural Characterization

The porous texture of carbon materials was characterized by nitrogen adsorption at 77k (Quantachrome Autosorb-1). A Hitachi S-4800 scanning electron microscope (SEM) equipped with field emission gun and a JEOL 2100 transmission electron microscopes (TEM) were employed for microstructural characterization. X-ray photoelectron spectroscopy (XPS) was obtained using an Axis Ultra spectrometer. The N 1s core level is fitted using CasaXPS software. Before XPS analysis, the samples were dried at 110 °C in vacuum oven over night to remove the absorbed water. To evaluate electrical conductivity, the carbon powders mixed with 10 wt% binder were pressed into a thin film of 100-200 µm in thickness, under a pressure of 100 MPa. Then the film resistances were measured using a four point electrical probe (Pro4 from Lucas Laboratories).

Results and discussion

Synthesis of highly functionalized activated carbons

This study focused on creating and testing carbons with a unique combination of both high heteroatom functionality and a high surface area, henceforth termed Highly Functionalized Activated Carbons, or HFAC. A commercially purchased high surface area activated carbon (NORIT® A SUPRA) was employed as a baseline, and is labeled AC. The physical and chemical properties of eggs have been thoroughly studied by food chemists. Egg white contains around 90% water and 10% proteins, including ovalbumin, ovotransferrin, ovomucoid and small amount of other proteins. Unlike plant-based precursors, these proteins are naturally rich in nitrogen, containing on the average 15% N by weight.[38] **Scheme S1** illustrates the entire preparation process for HFAC. Denaturation occurs upon adding ethanol, with the proteins subsequently loosing solubility in the water. Heating at 650°C in argon converts the denatured proteins into a low surface area carbon that retains a high fraction of the initial N content, termed highly functionalized carbon (HFC).

The chemical activation process was performed in argon at 550 °C, employing a mixture of carbon to KOH in 1:1, 1:2 and 1:3 weight ratios. The products are therefore named HFAC1, HFAC-2, and HFAC-3, with HFAC-3 employing the most KOH. The

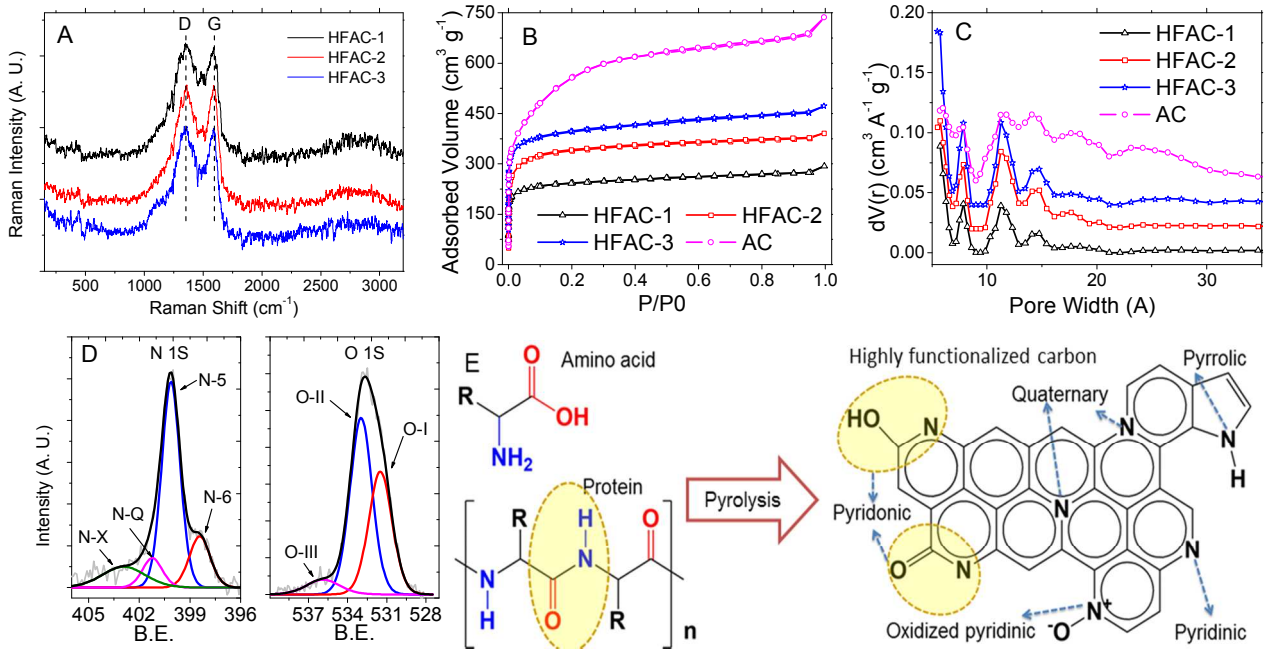

Fig. 2 (A) Raman spectra of HFAC materials; (B) Nitrogen adsorption isotherms at 77k and (C) NLDFT pore-size distribution HFACs and of AC; (D) N 1S and O 1S core level XPS spectra fitting of HFAC-2; (E) A schematic illustration of the typical N-containing groups in the precursor egg white protein and of N-functionalities in HFAC.

Cite this: DOI: 10.1039/c0xx00000x

www.rsc.org/xxxxxx

ARTICLE TYPE

Table 1 Physical and electrical properties of HFAC, including the unactivated HFC sample, and the baseline activated carbon AC.

	S_{BET}	S_{micro} [a]	V_{total} [b]	Composition [c]			Composition [d]				Conductivity	$C_{H_2SO_4}$ [e]		C_{KOH} [f]	
	[m^2g^{-1}]	[m^2g^{-1}]	[cm^3g^{-1}]	C %	N %	O %	C %	N %	O %	H%	[S m^{-1}]	[Fg^{-1}]	[μFcm^{-2}]	[Fg^{-1}]	[μFcm^{-2}]
HFC	17.8	2.2		82.1	8.4	9.5	76.1	8.7	8.7	2.1					
HFAC-1	521.0	459.1	0.38	82.0	7.3	10.7	74.5	7.6	13.1	2.4	124	273	52.4	227	43.6
HFAC-2	1217.1	1073.5	0.46	78.5	6.3	15.2	71.1	6.5	16.5	3.5	102	556	45.7	525	43.1
HFAC-3	1405.6	1211.3	0.73	82.2	4.2	13.6	74.1	4.1	16.0	3.7	75	420	29.9	409	29.1
AC	1840.3	1186.7	1.17	95.5		4.5					43	180	9.8	182	9.9

[a] surface area of micropores calculated by t-plot method; [b] total pore volume; [c] weight percent of elements obtained from XPS analysis; [d] weight percent of elements obtained from combustion analysis; [e], [f] Capacitance obtained at current density of 0.25 A g^{-1} in 1M H_2SO_4 and 1M KOH.

KOH activation of carbon is one of most frequently used activation method in industry. In general, low temperature (500-700 °C) activation will generate mainly micropores while high temperature activation (700-1000 °C) will broaden the pore size distribution through the formation of additional mesopores.[39] Our primary consideration for employing a low activation temperature was to preserve the N-functionalities, in addition to maximizing ion accessible porosity. For N-rich carbon, the N-content is very sensitive to the activation temperature. The effect of KOH in eliminating the N functionalities at high temperature is well demonstrated for the case of polyryrrole-derived carbons.[40] With an activation temperature increase from 600 °C to 800 °C, more than 80% of N will be eliminated.[41] For our materials, a significant amount of N-functionalities (about 30%) is lost even when a slightly higher temperature (600 °C) is employed.

Structure, porosity and surface chemistry of HFAC

Fig. 1A shows a representative SEM micrograph of HFAC-2, with the HFAC-1 and HFAC-3 specimens having an analogous macroscopic morphology. After carbonization and activation, the specimens are morphologically monolithic, with minimal macroporosity. This is quite different from the highly macroporous structure of conventional activated carbons. The dense morphology of HFAC is seen in the inset of **Fig. 1A**. The volume of HFAC-2 is about half of the baseline AC with same weight. When made into electrode with mass loading of 10 mg cm^{-2} under pressure of 100 MP, HFAC-2 is 85 µm in thickness (**Fig. S1A**), also about half of baseline AC (160µm, **Fig. S1B**). **Fig. 1B-D** show HRTEM micrographs of HFAC-1, HFAC-2 and HFAC-3 specimens, respectively. The contrast of the HRTEM images in all the specimens is consistent with that of structurally defective microporous carbons with only local aromatic ordering. The degree of ordering in a carbon is estimated by the intensity ratio between the G band (~1600 cm^{-1}) and the D band (~1350 cm^{-1}) of the Raman spectra.[42] The former corresponds to the graphitic order, while the latter corresponds to the degree of disordered/defectiveness in the structure. The amount of KOH employed in the activation process does not seem to affect the amount of order in these materials, with all the HFAC carbons showing a similar I_G/I_D ratio of around 1. The broad (200) X-ray diffraction peaks (**Fig. S1C**) confirm the low degree of order in these carbons, which is understandable since they are both carbonized and activated at low temperatures.

The porous texture of HFAC was analyzed by N_2-adsorption at 77K. **Fig. 2B** shows that all three carbons exhibit type I isotherms with well-defined plateaus; a typical character of microporous materials. The reference AC shows a broad knee in the low-pressure range indicating the existence of significant amount of mesopores. **Fig. 2C** shows the pore size distributions (pore width) as calculated by non-local density functional theory (NLDFT) model. The majority of the pores in the three HFAC specimens are in the sub 1.5 nm range. However, HFAC-2 and HFAC-3 demonstrate a higher pore contribution in the range of 1.5-2 nm, while HFAC-3 shows the presence mesopores that are in the range of 2-3 nm. **Table 1** lists the BET surface area and the total pore volume of the carbons. The HFC specimen (carbonized but not activated) has a very low surface area and pore volume. Going from HFAC-1 to HFAC-2 to HFAC-3 the surface area increases from 722.9 to 1217.1 and 1405.6 m^2 g^{-1}, while the total pore volume increases from 0.38, to 0.46 and 0.73 cm^3g^{-1}. A calculation by the t-plot method shows that more than 85% of the surface area of these carbons is from micropores. The baseline AC possesses a surface area of 1840.3 m^2 g^{-1}, with 1186.7 m^2 g^{-1} being associated with micropores. The electrical conductivity of each carbon is listed in Table 1. HFAC-1 displays the best conductivity of the lot (124 S m^{-1}), about 3 times higher than the conductivity of reference AC (43 S m^{-1}). The conductivity of HFAC-2 (102 S m^{-1}) and HFAC-3 (75 S m^{-1}) is also significantly improved relative to AC. This enhancement has been attributed to the doping effect of electron-rich N in a graphitic layer. [29]

Combustion elemental analysis and XPS were employed to obtain the bulk and surface heteroatom content. The amount N and O heteroatoms, determined by the combustion elements analysis is listed in **Table 1**. Prior to activation the carbon contains 8.7 wt% nitrogen and 8.7 wt% oxygen. The N-content is quite sensitive to the relative amount of KOH employed during

Table 2 Relative surface concentrations of nitrogen and oxygen species obtained by fitting the N 1S and O 1S core level XPS spectra.

	% of total N 1s				% of total O 1s		
Functionality	N-Q	N-5	N-6	N-X	O-I	O-II	O-III
B. E. (eV)	400.8	399.7	398.0	402.5	531.0	532.4	535.4
HFC	18.78	40.70	30.42	10.1	54.03	31.22	17.76
HFAC-1	12.54	57.82	17.42	12.22	31.51	58.57	9.92
HFAC-2	9.25	59.52	16.95	14.25	39.47	53.70	6.82
HFAC-3	8.08	62.41	18.31	11.38	38.38	57.24	4.38

activation, decreasing from 7.6 % for HFAC-1, to 6.5 % for HFAC-2 and 4.1 % for HFAC-3. For comparison, activating at 600 ^{o}C and 700 ^{o}C, using a KOH to carbon ratio of 2, decreased the N content to 3.5% and 1.4%. Those samples were not tested further. The HFACs also possess a substantial O content, up to 16.5%. From the XPS survey (**Fig. 2D**), it can be concluded that the HFAC surface contains mainly nitrogen (B.E. ~ 400 eV) and oxygen (B.E. ~ 530 eV) besides carbon (B.E. ~ 285eV) with no other heteroatoms being observable. A comparison of XPS and combustion analysis results indicates that the surface N content is quite comparable with the bulk, while the O content is slightly depleted.

The high-resolution N 1s and O 1s XPS spectra of HFAC-2 are shown in **Fig. 2D**, with the same results for HFAC-1, HFAC-3, and HFC (carbonized but not activated) being displayed in **Fig. S2**. The high-resolution N 1s core level spectra can be deconvoluted by 4 peaks representing pyridinic N (N-6 at 398.0±0.2 eV), pyrrolic or pyridonic N (N-5 at 399.7±0.2 eV), quaternary N (N-Q at 400.8±0.2 eV) and oxidized N (N-X at 402.5±0.2 eV) (**Fig. S2**).[42, 43] The typical structure of these five N functionalities is illustrated in **Fig. 2E,** while the percentage of each component is listed in **Table 2**.

The pyridonic N functionalities have a tautomer with hydroxypyridine-like structures. The HFACs contain proportionally less N-Q groups as compared to HFC. This indicates that some of the N functionalities that were originally located in the middle of the highly defective aromatic rings are converted into N sitting on edge sites or more likely are preferentially eliminated during the activation process. Another notable change is the activation-induced drop in the N-6 content and an increase in the N-5 content. We observed this trend in another study, where a N-rich carbon was activated in air.[44] This suggests that a portion of the pyridinic N functionalities have converted into pyridonic N, since a conversion into pyrrolic N (associated with a carbon framework change from a 6 member ring to a 5 member ring), would require substantially higher activation energy. In addition, it has been demonstrated that at high temperatures the pyridinic N functionalities are more stable than pyrrolic N functionalities.[45] Therefore a conversion from pyrrolic N to pyridinic N is unlikely to occur.

The portion of N-5 functionalities in all HFAC samples (57.82-62.41%) is considerably higher than what was measured for N-rich carbons derived from other precursors.[27, 28] Even in the as-carbonized HFC specimen, N-5 takes more than 40% of total N functionalities. This may be related to the structure of the protein precursor. As illustrated in **Fig. 2E**, a protein is composed of various amino acids linked together by peptide links. These peptides are the dominant N-containing portion of a given molecule. The structure of this four-atom functional group is almost identical to the structure of pyridonic N functionalities, where the N atom is connected to an H atom, while the adjacent C atom is connected with an O atom through double bond. It is known that the structure of N-containing groups in the precursor does have some influence on the resultant N moieties. For example, carbons derived from polypyrrole are observed to contain more pyrrolic N functionalities.[46, 47] It is therefore reasonable to argue that it is the peptide links in the protein precursor that yield the large percentage of pyridonic N functionalities in the resultant HFC and then in the HFAC.

As Table 2 demonstrates, activation also increases the amount of oxygen in the materials. According to the high-resolution O 1s core level spectra (**Fig. S2**), there are generally three types of O functionalities: C=O groups (O-I at 531.0±0.2 eV), C-OH and/or C-O-C groups (O-II at 532.4±0.2 eV) and carboxylic groups (O-III at 535.4±0.2 eV). In all the carbons, O-I and O-II are the dominant functionalities However after activation the portion of O-I groups significantly decreases, while the portion of O-II increases. It is widely accepted that the O functionalities on carbons contribute to the pseudocapacitance through quinone/hydoquinone redox pair.[21, 48]

Electrochemical behavior of HFAC carbons in 3-electrode setup

We tested HFCA materials in both acidic (1M H_2SO_4) and basic (1M KOH) electrolytes, using a three-electrode setup. A potential window of 1V was employed for these tests. To understand the electrochemical behavior of the carbons at different potential, the cyclic voltammograms (CVs) were recorded, using a scan rate of 5mV/s. These results are shown in **Fig. 3A-B**. The baseline AC electrode demonstrates the expected quasirectangular CV associated with charge storage by the formation of an electrical double layer (EDLC), with only a minor redox hump present due the 4.5% surface oxygen. In contrast, the CVs of all three HFACs show prominent redox peaks that are in effect overlaid on top of a substantial EDLC component. Since HFACs possess a high surface area in addition to high surface heteroatom functionality, a significant EDLC contribution is expected. The redox peaks are centered at -0.1 to 0 V (vs. Hg/$HgSO_4$) in H_2SO_4 and at -0.6 to -0.5V (vs. Hg/HgO) in KOH. These prominent peaks reveal a major pseudocapacitive contribution from the surface redox reactions of the N and O functionalities.

The significant redox contribution in HFACs also causes a distortion of the galvanostatic charge/discharge curves, as compared to the almost perfect triangular shape of baseline AC. This is shown in **Fig. 3C**, where the specimens were tested at 0.5A g^{-1}. Similarly to the CV results, the HFAC-2 shows the highest capacitive current and the most developed redox hump. None of the specimens demonstrate significant IR drops upon discharge, indicating that they are quite electrically conductive. Moreover in both acid and base, the time to charge is equivalent to the time to discharge (*e.g.* for HFAC-2 958 s *vs.* 964 s in H_2SO_4), indicating excellent coulombic efficiency. Calculated by

Cite this: DOI: 10.1039/c0xx00000x

www.rsc.org/xxxxxx

ARTICLE TYPE

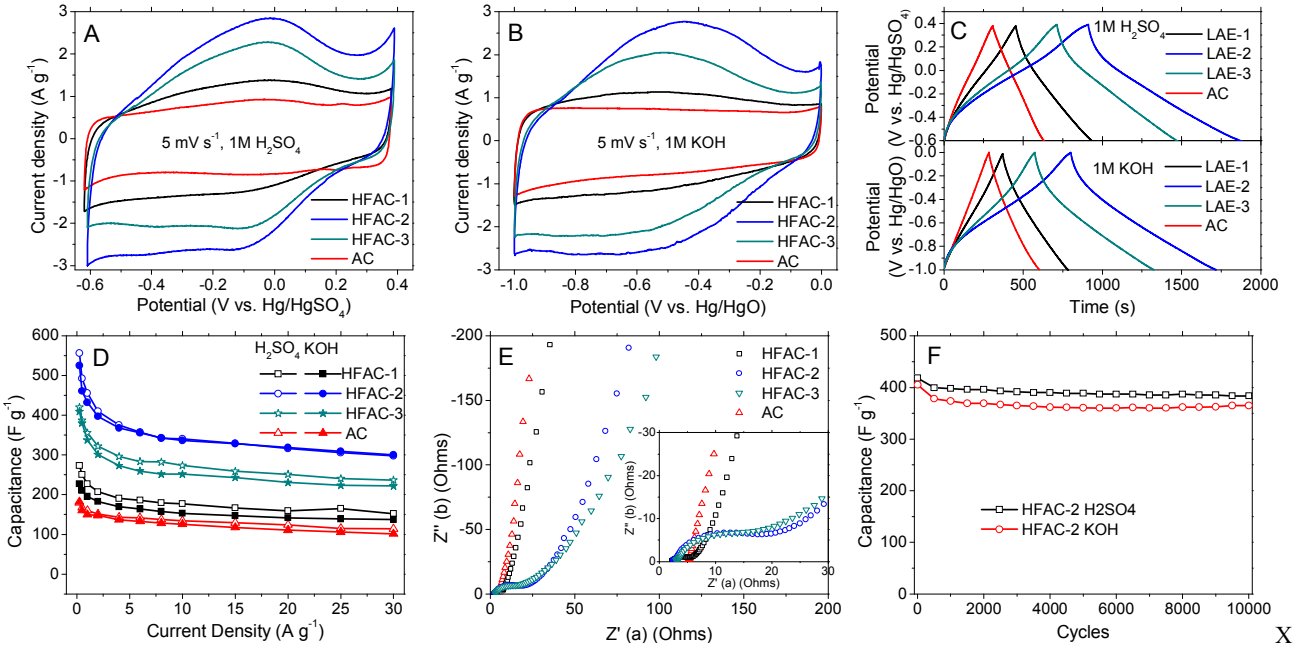

Fig.3 Electrochemical performance of HFACs in three-electrode setup. (A) Cyclic voltammograms (CVs) in 1M KOH; (B) CVs in 1M H_2SO_4; (C) galvanostatic charge/discharge curves at 0.5A g^{-1}; (D) gravimetric capacitances measured at various charge/discharge current densities; (E) Nyquist plots in 1M H_2SO_4; (F) the evaluation of specific capacitance *versus* the number of cycles, tested at 2 A g^{-1}.

the galvanostatic charge/discharge curves recorded at 0.5 A g^{-1}, the capacitances of HFAC-1, HFAC-2 and HFAC-3 are 250, 481 and 387 F g^{-1} in H_2SO_4, and 211, 445 and 380 F g^{-1} in KOH. The measured densities of the electrodes based on HFAC-1, HFAC-2 HFAC-3 and AC (pressed at 100 MPa) are 1.5, 1.1, 0.86 and 0.6 g cm^{-3}, respectively. Thus the calculated volumetric capacitance of HFAC-2 is 611 F cm^{-3} in H_2SO_4, and 578 F cm^{-3} in KOH. This is 5 - 6 times higher than the volumetric capacitance of the reference AC, which is 108 F cm^{-3} in either electrolyte.

As shown in **Table 1**, the surface area normalized capacitance of HFAC-2 (45.7 μF cm^{-2}) is more than 4 times of that of AC (9.9 μF cm^{-2}) and is much higher than the theoretical EDLC capacitance of carbon (10-25 μF cm^{-2}).[3] To estimate the pure EDLC contribution to the overall capacitance, we eliminated the N and O functionalities of HFAC-2 by annealing the sample at 1100°C for 2 hours in argon (sample labeled HFAC-2-1100). This treatment reduced the N and O content to 1.7 % and 2.0 %. The specific surface area also decreased from 1217 $m^2 g^{-1}$ to 859 $m^2 g^{-1}$, while the relative pore size distribution remained almost unchanged. This is shown in **Fig. S4**. The CV of HFAC-2-1100 is plotted in **Fig. S5 A** along with HFAC-2 and AC. The HFAC-2-1100 exhibits a much more narrow and box-like CV without any humps. The specific capacitance dramatically drops to 92 F g^{-1}, corresponding to a surface area normalized capacitance of 10.7 μF cm^{-2}. Therefore we can argue that *on a surface area normalized basis*, the ratio of faradaic *versus* EDLC capacitance is roughly 3:1, *i.e.* (45.7-10.7):10.7 μF cm^{-2}. The EDLC contribution to the capacitance in HFAC-2 may also be estimated by examining the galvanostatic charge/discharge curves and the CV curves.[49] At high potentials, where the redox humps are clearly exhausted in the CV, the measured charge may be assumed to be primarily caused by reversible ion adsorption/desorption. Were one to examine the galvanostatic data, it would be evident that the purely EDLC portion of the curve has a distinctly different slope than the combined faradaic + EDLC portion. The actual amount of charge associated with the EDLC region is most readily calculated from the discharge galvanostatic curve, within that voltage window where the slope is markedly steeper. According to **Fig. S5 B**, one can attribute the 0.4 to 0.2 V *vs.* $Hg/HgSO_4$ range to EDLC capacitance, and 0.2 to -0.6 V to EDLC combined with reversible faradaic reactions. This yields a value of 118 F g^{-1} for EDLC and 363 F g^{-1} for faradaic, *i.e.* the same ratio of 1:3. This agrees with previous studies where researchers have demonstrated the dominance of functional groups in the overall capacitive response. [26, 28]

Fig. 3D shows the gravimetric capacitance of all HFAC- and AC electrodes as a function of current density. Even at a very high charging rate of 30 A g^{-1}, HFAC-2 still provides a capacitance of 297 F g^{-1} in H_2SO_4. This is almost 3X the value for AC at the same scan rate. A factor of 3 is also the difference in the specific capacitances at a low current density (*e.g.* 0.25 A g^{-1}), indicating that both materials possess analogous rate sensitivity.

Table 3 Specific capacitance of HFACs *versus* recently published state-of-the-art carbons, all tested in a 3-electrode configuration.

Carbon Type	C [a] F g^{-1}	**R** [b] Ag^{-1}	**V** [c]	El [d]	Ref
HFAC	*525*	*0.25*	*1.0*	*KOH*	*This work*
HFAC	*556*	*0.25*	*1.0*	*H_2SO_4*	*This work*
Porous N-doped CNT	220	0.5	1.0	KOH	47
Functionalized carbon	319	0.5	1.0	KOH	40
Hair-Derived Carbon	340	2	1.0	KOH	35
Nitrogen-doped graphene	280	<1	0.8	KOH	23
Leaves derived carbons	400	0.5	1.0	KOH	34
Partially reduced GO	347	0.2	1.0	H_2SO_4	24
N-Containing HTC	300	0.2	1.0	H_2SO_4	26
Polymer derived carbon	700	0.1	0.7	H_2SO_4	31
Carbon-nanotube aerogel	524	0.2	1.0	KOH	18
Graphene-CNT architecture	326	7 [e]	1.0	H_2SO_4	19
Bacteria promoted carbon	327	1	1.0	H_2SO_4	33
Zeolite templated carbon	340	0.1	1.2	H_2SO_4	42

[a] Specific capacitance; [b] current density; [c] potential window; [d] electrolyte type; [e], the value was estimated from the CV.

Fig. 3E shows the Nyquist plots of the electrodes. After fitting the Nyquist plots with the typical circuit model (**Fig. S6**), it can be concluded that the HFAC materials actually possess lower equivalent series resistances. For HFAC the equivalent series resistance R_{es} ranges from 2.03 - 3.28 Ω, while for AC it is 5.18 Ω. This is attributed to the known role of bulk N in increasing a carbons' electrical conductivity. [29] A secondary important factor leading to a lower Res may be the decreased interparticle contact resistance of an electrode packed with the more dense macroscopically block-like HFAC (**Fig. 1A**). The charge transfer resistance of HFACs (*e.g.* 18.07 Ω for HFAC-2) is higher than of AC (0.25 Ω). This is expected since for HFAC's charge transfer involves surface redox processes that are less facile than pure EDLC. The cycle life of HFAC-2 was evaluated by galvanostatic charge/discharge at 2 A g^{-1}. As **Fig. 3F** shows, after 10,000 cycles in H_2SO_4 and KOH, the HFAC-2 loses only 8.2% and 9.4% of its initial capacitance, respectively.

The HFACs very favorable performance may be attributed to a synergy of the high surface area with ample microporosity and the high surface N and O content both on the surface and in the bulk. For some low surface area carbons that are very rich in N surface groups, the surface area normalized specific capacitance may be extremely high, *e.g.* 3300 μF cm^{-2}. [28, 50] Such extraordinarily high surface area normalized capacitance usually does not translate into a analogously impressive specific capacitance due to the low specific surface area of such materials. In our case, however, the total surface area of HFCA-2 and HFCA-3 is almost on par with AC. The HFCAs are primarily microporous, with net micropore surface area actually being higher in HFAC-3 than in AC (1211.3 m^2 g^{-1} *vs.* 1186.7 m^2 g^{-1}). This high content of microporosity in HFACs is advantageous for increasing the materials' specific capacitance in an aqueous electrolyte, since it is known to be more effective than mesoporosity for maximizing the adsorption of ions at scan rates where diffusion limitations are not significant.[51, 52]

As mentioned, the HFAC electrodes are highly electrically conductive, which is expected in materials rich in bulk N. This reduces the IR losses in the specimens, especially at high current densities. Table 2 shows that more than 75% of the N-functionalities in HFACs are from N-6 and N-5. There have been several arguments put fourth regarding to the role of the different N-functionalities in determining electrochemical performance of the carbons. [32, 50, 53] One of the more detailed mechanisms has been proposed by authors in ref.[54] Combining the XPS results and first principles calculations, they argue that the conversation between pyridonic and pyridinic N functionalities, where a transfer of two electrons is involved, is the key redox pair in the pseudocapacitance response of N-rich carbons. It is worth is point out that the N-rich carbons derived from protein[37, 44] or other N-rich biomass[21, 26] are generally gives much better developed redox peaks on CVs and also higher surface area normalized specific capacitance than those carbons derived from polyryrrole.[40] We believe that this observation supports the authors' argument that pyridonic N functionalities are more electroactive than pyrrolic N functionalities. [54]

Examining the morphology (**Fig. S1** and **1A**) and the relatively low total pore volume of HFACs highlights an additional advantage of the materials: In the dry state, macroscopic voids per se do not add extra weight to the system. However in a real working cell the situation is different since pores become filled with electrolyte. A "fluffy" carbon full of macroporosity will not only unnecessary increase the electrode volume, but will also add to the system weight since it will be carrying more electrolyte than a comparable microporous material that is macroscopically monolithic. Researchers have therefore argued that a high surface area material but with a low total pore volume is highly desirable.[52, 55] The way to achieve this is by minimizing the macropore and large mesopore content, without sacrificing micropores/small mesopores. SEM and BET analysis of HFACs indicates that we were successful in achieving this. For instance, the surface area associated with micropores is on par for AC and HFAC-2 (1186.7 *vs.* 1073.5 m^2 g^{-1}), while the total pore volume is 154% larger in the former (1.17 *vs.* 0.46 cm^3 g^{-1}). The HFAC-3 specimen actually has a higher surface area associated with microporosity than AC (1211.3 *vs.* 1186.7), despite the AC possessing 60% larger pore volume (1.17 *vs.* 0.73 cm^3 g^{-1}). The N-rich surfaces of the HFACs are also hydrophilic, promoting deep wetting by the electrolyte into the micron-scale particles and making more inner surfaces ion accessible.

Table 3 shows a comparison of the specific capacitance of HFACs *versus* recently published high performance heteroatom-rich carbons, all tested in a 3-electrode configuration. The table also lists the voltage range employed, since for a total amount of charge stored Q, the capacitance C is inversely proportional to the window employed, *i.e.* $C = Q/\Delta V$. In general, HFAC shows one of the most promising specific capacitances in literature, especially when considering an "apples to apples" comparison for systems that employ a window of 1V.

Electrochemical behavior of HFAC in an asymmetric hybrid cell

The premise we put fourth in the Introduction was that since a vast amount of research has been performed and major advances have been made in improving the capacitive properties of the positive electrode in a hybrid asymmetric cell, it would be highly desirable to boost the performance of the negative electrode to match. With a specific capacitance of over 550 F g^{-1}, HFACs are ideally suited for this purpose. To evaluate the performance of HFACs, we employed a $NiCo_2O_4$/graphene nanocomposite as positive electrode. This intermediate capacitance material was

Cite this: DOI: 10.1039/c0xx00000x

www.rsc.org/xxxxxx

ARTICLE TYPE

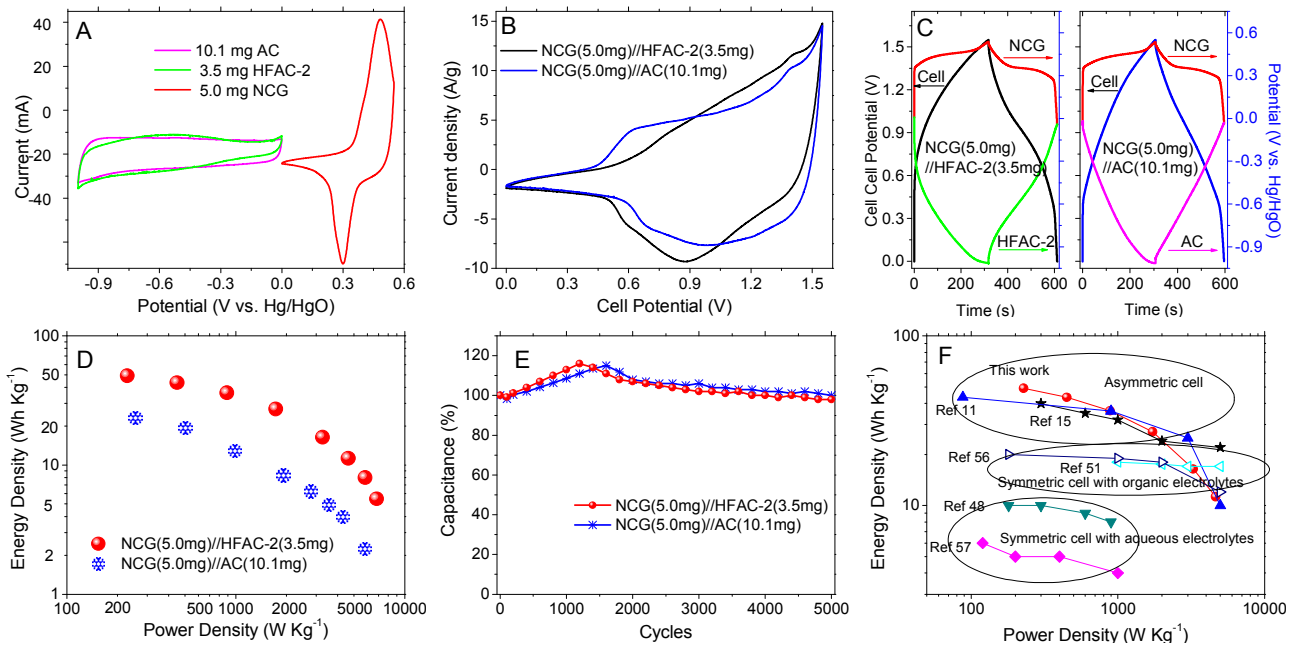

Fig. 4 Comparative electrochemical performance of asymmetric supercapacitor cells that employ the same positive electrode $NiCo_2O_4$/graphene nanocomposite (NCG), but with a different negative electrode (HFAC-2 *vs.* baseline AC), tested in 1M KOH. (A) CVs of the individual electrodes, tested in a 3-electrode setup at 5 mV s^{-1}; (B) CVs of the two asymmetric full cells; (C) galvanostatic charge/discharge curves of the two asymmetric cells at 0.5A g^{-1}, and the in-situ tracked variation of the potential in each individual electrode; (D) Ragone plots of the asymmetric cells, presented on an active mass normalized basis; (E) full asymmetric cell percent capacitance retention *versus* the number of cycles, tested at 2 A g^{-1}; (F) Performance comparison of the HFAC-NCG cell *versus* state-of-the-art asymmetric supercapacitors previously reported in literature, and *versus* representative high performance carbon-based symmetric cells employing aqueous and organic electrolytes. All energy-power values are presented on an active mass normalized basis.

demonstrated to have the highly advantageous feature of being usable at commercial or near commercial level mass loadings (up to 10 mg cm^{-2}), allowing for the fabrication of working cells that are relatively commercially representative. [13] As shown in **Fig. S7**, the nanocomposite is composed of metal oxide "nano-needles" with grain sizes in the 10-20 nm range intimately interspersed with the graphene nanoflakes that are several nanometers in thickness. The material exhibits capacitances ranging from 650 F g^{-1} to 400 F g^{-1} at the pertinent scan rates, with a potential window of 0 to 0.55 V *vs.* Hg/HgO. The XRD pattern of this material is shown in **Fig. S8**, with additional microstructural details being provided in our previous publication.[13]

In the current study we employed 5.0 mg cm^{-2} of $NiCo_2O_4$/graphene (labeled in figures as NCG) as the positive electrode. To obtain proper capacitance matching 3.5 mg cm^{-2} of HFAC-2 or 10.1 mg cm^{-2} of AC were employed to make the negative electrode. The electrolyte employed was KOH, which is considered optimum for large-scale stationary applications of hybrid devices. **Fig. 4A** shows the CVs of each individual electrode, in a 3-electrode setup, tested within the target voltage range of the asymmetric cell. It can be observed that the 3.5 mg of HFAC-2 (electrode area ~ 1 cm^2) provides almost the same total capacitive current as the 10.1 mg of AC. Similarly, as shown by the CVs in **Fig. 4B**, cells with either 3.5 mg of HFAC-2 or 10.1 mg of AC opposing 5.0 mg of $NiCo_2O_4$/graphene will generate nearly the same total capacitive current. The HFAC-2 electrode therefore results in the same cell capacitance as the AC, but with a total active mass reduction of 44% for a full cell (15.1 mg *vs.* 8.5 mg). The CVs do show a difference in their shape, caused by the N and O redox reactions on HFAC-2. **Fig. 4C** shows the galvanostatic charge/discharge curves of asymmetric cells with the potential change of each individual electrode in-situ monitored by an auxiliary channel. For consistency, in each cell the charge/discharge current passing through the positive electrode was kept a 2.5 mA (*i.e.* 0.5 A g^{-1}). During the charge/discharge, the positive electrode is actually swinging between 0 and 0.53 V *vs* Hg/HgO, while the HFAC-2 between 0 and -1.02 V *vs* Hg/HgO. With the precisely calculated mass and countered with identical positive electrode, HFAC-2 gives the same capacitance as AC with only about 1/3 mass. By replacing AC with HFAC-2, the specific capacitance of whole cell greatly enhanced from 64.0 F g^{-1} to 113.8 F g^{-1} and the energy density at 250 W kg^{-1} also increased from 23 Wh $kg^{-1}$to 48 Wh kg^{-1} (**Fig. 4D**). In terms of volumetric energy density, the improvement is even more significant. Given the aforementioned densities of carbons and the density of $NiCo_2O_4$/graphene (2.3 g cm^{-3}), the calculated energy density of HFAC-2 based asymmetric cell is

Cite this: DOI: 10.1039/c0xx00000x

www.rsc.org/xxxxxx

ARTICLE TYPE

Table 4 A performance comparison for state-of-the-art carbon negative electrodes employed to oppose positive Ni/Co oxides in asymmetric supercapacitor cells.

Asymmetric Cell	Carbon Type	C_{carbon} F g^{-1}	$C_{positive}$ F g^{-1}	C_{cell} F g^{-1}	V_{cell} V	ED [a] Wh kg^{-1}	Ref
$NiCo_2O_4$/graphene//HFAC	*N-rich carbon*	***525***	*600*	*114*	*1.55*	*48*	*This work*
$NiCo_2O_4$/graphene//AC	*Activated carbon*	***182***	*600*	*64*	*1.55*	*23*	*This work*
CoO@PPy//AC	Activated carbon	**120** [b]	2223	80 [b]	1.8	43.5	11
Ni–Zn–Co oxide //carbon	Porous carbon	**196**	946	136	1.5	41.7	17
$Ni(OH)_2$/CNT//AC	Activated carbon	**120**	3300	112.5	1.8	50.6	10
NiO//rGO	Reduced graphene oxide	**210**	392	50	1.7	39.9	15
Co_3O_4-rGO//AC	Activated carbon	**210**	636	114	1.5	35.7	16
NiO//carbon	Porous carbon	**100**	750 [b]	37	1.5	16.6	14

[a] maximum energy density reported by authors; [b] estimated values from published graphs..

76.3 Wh L^{-1}, which is 4 times higher than 18.3 Wh L^{-1} of the AC based asymmetric cell. Proper capacitance match between positive and negative electrodes are critical to achieve the maximized performance. In a control experiment with all the electrodes at the same mass loading (5.0 mg, on 1 cm^2 electrode), the cell with HFAC-2 as negative electrode exhibits a specific capacitance of 84 F g^{-1}, while the cell with AC has a specific capacitance of 47 F g^{-1}. However, only a potential window of 1.4 V can be achieved (**Fig. S9).**

Fig. 4E shows the cycling stability of both cells, indicating that after 5,000 cycles there is less than 2% reduction in the specific capacitance. The $NiCo_2O_4$/graphene electrode is known to be cyclically stable (no degradation at 5K cycles) because of its interconnecting graphene backbone. The slightly capacitance increasing of cells in the first 1000-2000 cycles is due to the further activation of $NiCo_2O_4$. The fact that cells with the faradaic HFAC are as stable as the cells employing EDLC-based AC is a testament to the utility of employing carbons with a rich *bulk* heteroatom content that ensures that the surface functionality is not eliminated by cycling. **Fig. 4F** compares the performance of the HFAC-2 based asymmetric supercapacitor in comparison with other state-of-the-art asymmetric supercapacitors. The figure also presents energy-power combinations for literature reported high performance carbon-based symmetric cells employing aqueous and organic electrolytes. All energy-power values are presented on an active mass normalized basis.

Table 4 provides performance numbers for the closely related published systems based on negative electrode carbons and positive electrode Ni/Co oxides. The asymmetric supercapacitors exhibit significantly higher energy densities as compared to the symmetric ones operating in either aqueous or organic electrolytes. [48, 51, 56, 57] More importantly, even compared with asymmetric systems based on positive electrodes with much a higher specific capacitance (*e.g.* 3300 F g^{-1}), HFAC-2 remains quite competitive. For instance, as Table 4 shows the cell composed of activated carbon opposing the 3300 F g^{-1} $Ni(OH)_2$/CNT yields a maximum energy density of 50.6 Wh kg^{-1}, while our system yields 48 Wh kg^{-1}.

Conclusions

Heteroatom functionalized carbon-based materials are attracting intense attention in the electrochemical capacitor and secondary battery scientific community due to their exceptional surface area normalized charge storage properties. We employed a template-free facile synthesis process to convert biomass-derived proteins into macroscopically dense, yet highly porous (surface area over 1400 m^2 g^{-1}, with 88% microporosity by volume), highly functionalized (6.7% N and 16.5% O) carbons. These materials, termed Highly Functionalized Activated Carbons or "HFAC", exhibit a capacitance as high as 556 F g^{-1}, which is among the highest reported for any carbon. The HFACs serve as ideal negative electrodes in asymmetric hybrid supercapacitors, with cells employing HFACs demonstrating 2X higher specific energy as compared to a cell employing a commercial activated carbon and the same $NiCo_2O_4$/graphene positive electrode. On a Ragone chart the HFAC//$NiCo_2O_4$/graphene cell is competitive with the best literature published asymmetric systems, including the ones based on positive electrodes with a specific capacitance higher by a factor of five.

Acknowledgements

Funding by ALMA/AB Bio, NSERC and NINT NRC.

Notes and references

[a] *Chemical and Materials Engineering, University of Alberta, 9107 - 116 St., Edmonton, AB, T6G 2V4, Canada. Fax: (780)492-2881; Tel: (780)492-1542; E-mail: huanleiwang@gmail.com; dmitlin@ualberta.ca*
[b] *National Institute for Nanotechnology (NINT), NRC, 11421 Saskatchewan Dr., Edmonton, AB, T6G 2M9,Canada*

† Electronic Supplementary Information (ESI) available: [details of any supplementary information available should be included here]. See DOI: 10.1039/b000000x/

1 C. Liu, F. Li, L. P. Ma and H. M. Cheng, *Adv. Mater.*, 2010, **22**, E28; P. Simon and Y. Gogotsi, *Nat. Mater.*, 2008, **7**, 845; W. Gu and G. Yushin, *WIREs Energy Environ.*, 2013, 10.1002/wene.102.
2 C. Xu, B. Xu, Y. Gu, Z. Xiong, J. Sun and X. S. Zhao, *Energy Environ. Sci.*, 2013, **6**, 1388.
3 B. E. Conway, *Electrochemical supercapacitors : scientific fundamentals and technological applications*, Plenum Press, New York, 1999; H. Jiang, P. S. Lee and C. Li, *Energy Environ. Sci.*, 2013, **6**, 41.

4 L. L. Zhang and X. S. Zhao, *Chem. Soc. Rev.*, 2009, **38**, 2520.

5 J. W. Kim, V. Augustyn and B. Dunn, *Adv. Energy Mater.*, 2012, **2**, 141; X. H. Lu, T. Zhai, X. H. Zhang, Y. Q. Shen, L. Y. Yuan, B. Hu, L. Gong, J. Chen, Y. H. Gao, J. Zhou, Y. X. Tong and Z. L. Wang, *Adv. Mater.*, 2012, **24**, 938; H. J. Huang and X. Wang, *Nanoscale*, 2011, **3**, 3185; L. Q. Mai, F. Yang, Y. L. Zhao, X. Xu, L. Xu and Y. Z. Luo, *Nat. Commun.*, 2011, **2**.

6 H. W. Wang, Z. A. Hu, Y. Q. Chang, Y. L. Chen, H. Y. Wu, Z. Y. Zhang and Y. Y. Yang, *J. Mater. Chem.*, 2011, **21**, 10504.

7 Z. J. Fan, J. Yan, T. Wei, L. J. Zhi, G. Q. Ning, T. Y. Li and F. Wei, *Adv. Funct. Mater.*, 2011, **21**, 2366; J. T. Zhang, J. W. Jiang, H. L. Li and X. S. Zhao, *Energy Environ. Sci.*, 2011, **4**, 4009.

8 H. L. Wang, Y. Y. Liang, T. Mirfakhrai, Z. Chen, H. S. Casalongue and H. J. Dai, *Nano Res.*, 2011, **4**, 729.

9 Q. Cheng, J. Tang, J. Ma, H. Zhang, N. Shinya and L. C. Qin, *Carbon*, 2011, **49**, 2917; Z. P. Li, J. Q. Wang, S. Liu, X. H. Liu and S. R. Yang, *J. Power Sources*, 2011, **196**, 8160; Y. Cheng, H. Zhang, C. V. Varanasi and J. Liu, *Energy Environ. Sci.*, 2013, **6**, 3314; G. Q. Zhang, H. B. Wu, H. E. Hoster, M. B. Chan-Park and X. W. Lou, *Energy Environ. Sci.*, 2012, **5**, 9453; A. Boisset, L. Athouël, J. Jacquemin, P. Porion, T. Brousse and M. Anouti, *J. Phys. Chem. C*, 2013, **117**, 7408.

10 Z. Tang, C.-h. Tang and H. Gong, *Adv. Funct. Mater.*, 2012, **22**, 1272.

11 C. Zhou, Y. Zhang, Y. Li and J. Liu, *Nano Lett.*, 2013, **13**, 2078.

12 A. Sumboja, C. Y. Foo, X. Wang and P. S. Lee, *Adv. Mater.*, 2013, **25**, 2809; J. Ji, L. L. Zhang, H. Ji, Y. Li, X. Zhao, X. Bai, X. Fan, F. Zhang and R. S. Ruoff, *ACS Nano*, 2013, **7**, 6237; J. W. Long, D. Belanger, T. Brousse, W. Sugimoto, M. B. Sassin and O. Crosnier, *MRS Bull.*, 2011, **36**, 513; L. Estevez, R. Dua, N. Bhandari, A. Ramanujapuram, P. Wang and E. P. Giannelis, *Energy Environ. Sci.*, 2013, **6**, 1785.

13 H. Wang, C. M. B. Holt, Z. Li, X. Tan, B. S. Amirkhiz, Z. Xu, B. C. Olsen, T. Stephenson and D. Mitlin, *Nano Res.*, 2012, **5**, 605.

14 D.-W. Wang, F. Li and H.-M. Cheng, *J. Power Sources*, 2008, **185**, 1563.

15 F. Luan, G. Wang, Y. Ling, X. Lu, H. Wang, Y. Tong, X.-X. Liu and Y. Li, *Nanoscale*, 2013, **5**, 7984.

16 L.-J. Xie, J.-F. Wu, C.-M. Chen, C.-M. Zhang, L. Wan, J.-L. Wang, Q.-Q. Kong, C.-X. Lv, K.-X. Li and G.-H. Sun, *J. Power Sources*, 2013, **242**, 148.

17 H. Wang, Q. Gao and J. Hu, *J. Power Sources*, 2010, **195**, 3017.

18 T. Bordjiba, M. Mohamedi and L. H. Dao, *Adv. Mater.*, 2008, **20**, 815.

19 S. Y. Yang, K. H. Chang, H. W. Tien, Y. F. Lee, S. M. Li, Y. S. Wang, J. Y. Wang, C. C. M. Ma and C. C. Hu, *J. Mater. Chem.*, 2011, **21**, 2374.

20 D. Puthusseri, V. Aravindan, S. Madhavi and S. Ogale, *Energy Environ. Sci.*, 2014, **7**, 728.

21 E. Raymundo-Pinero, M. Cadek and F. Beguin, *Adv. Funct. Mater.*, 2009, **19**, 1032.

22 F. Beguin, K. Szostak, G. Lota and E. Frackowiak, *Adv. Mater.*, 2005, **17**, 2380; W. Gu, M. Sevilla, A. Magasinski, A. B. Fuertes and G. Yushin, *Energy Environ. Sci.*, 2013, **6**, 2465; A. L. Comte, G. Pognon, T. Brousse and D. Belanger, *Electrochemistry*, 2013, **81**, 863.

23 H. M. Jeong, J. W. Lee, W. H. Shin, Y. J. Choi, H. J. Shin, J. K. Kang and J. W. Choi, *Nano Lett.*, 2011, **11**, 2472.

24 Y. Chen, X. O. Zhang, D. C. Zhang, P. Yu and Y. W. Ma, *Carbon*, 2011, **49**, 573.

25 Y. C. Qiu, X. F. Zhang and S. H. Yang, *Phys. Chem. Chem. Phys.*, 2011, **13**, 12554; H. L. Guo and Q. M. Gao, *J. Power Sources*, 2009, **186**, 551.

26 L. Zhao, L. Z. Fan, M. Q. Zhou, H. Guan, S. Y. Qiao, M. Antonietti and M. M. Titirici, *Adv. Mater.*, 2010, **22**, 5202.

27 E. J. Ra, E. Raymundo-Pinero, Y. H. Lee and F. Beguin, *Carbon*, 2009, **47**, 2984.

28 D. Hulicova, J. Yamashita, Y. Soneda, H. Hatori and M. Kodama, *Chem. Mater.*, 2005, **17**, 1241.

29 P. Serp and J. L. Figueiredo, *Carbon materials for catalysis*, John Wiley & Sons, Hoboken, N.J., 2009.

30 L. L. Zhang, X. Zhao, H. Ji, M. D. Stoller, L. Lai, S. Murali, S. McDonnell, B. Cleveger, R. M. Wallace and R. S. Ruoff, *Energy Environ. Sci.*, 2012, **5**, 9618.

31 H. Zhu, X. Wang, X. Liu and X. Yang, *Adv. Mater.*, 2012, **24**, 6524.

32 B. Xu, S. Hou, G. Cao, F. Wu and Y. Yang, *J. Mater. Chem.*, 2012, **22**, 19088.

33 H. Sun, L. Cao and L. Lu, *Energy Environ. Sci.*, 2012, **5**, 6206.

34 M. Biswal, A. Banerjee, M. Deo and S. Ogale, *Energy Environ. Sci.*, 2013, **6**, 1249.

35 W. Qian, f. Sun, Y. Xu, L. Qiu, C.-H. Liu, S.-D. Wang and F. Yan, *Energy Environ. Sci.*, 2013.

36 Y. Mao, H. Duan, B. Xu, L. Zhang, Y. S. Hu, C. C. Zhao, Z. X. Wang, L. Q. Chen and Y. S. Yang, *Energy Environ. Sci.*, 2012, **5**, 7950.

37 Z. Li, Z. Xu, X. Tan, H. Wang, C. M. B. Holt, T. Stephenson, B. C. Olsen and D. Mitlin, *Energy Environ. Sci.*, 2013, **6**, 871.

38 T. Yamamoto, *Hen eggs : their basic and applied science*, CRC Press, Boca Raton, 1997.

39 J. Wang and S. Kaskel, *J. Mater. Chem.*, 2012, **22**, 23710.

40 L. Qie, W. Chen, H. Xu, X. Xiong, Y. Jiang, F. Zou, X. Hu, Y. Xin, Z. Zhang and Y. Huang, *Energy Environ. Sci.*, 2013, **6**, 2497.

41 M. Sevilla, P. Valle-Vigón and A. B. Fuertes, *Adv. Funct. Mater.*, 2011, **21**, 2781; M. Sevilla, R. Mokaya and A. B. Fuertes, *Energy Environ. Sci.*, 2011, **4**, 2930.

42 C. O. Ania, V. Khomenko, E. Raymundo-Pinero, J. B. Parra and F. Beguin, *Adv. Funct. Mater.*, 2007, **17**, 1828.

43 S. Biniak, G. Szymanski, J. Siedlewski and A. Swiatkowski, *Carbon*, 1997, **35**, 1799.

44 Z. Li, L. Zhang, B. S. Amirkhiz, X. H. Tan, Z. W. Xu, H. L. Wang, B. C. Olsen, C. M. B. Holt and D. Mitlin, *Adv. Energy Mater.*, 2012, **2**, 431.

45 Z. Lin, G. H. Waller, Y. Liu, M. Liu and C.-p. Wong, *Nano Energy*, 2013, **2**, 241; Z. Lin, M.-k. Song, Y. Ding, Y. Liu, M. Liu and C.-p. Wong, *Phys. Chem. Chem. Phys.*, 2012, **14**, 3381.

46 Z. Wang, X. Xiong, L. Qie and Y. Huang, *Electrochim. Acta*, 2013, **106**, 320; L. Qie, W. M. Chen, Z. H. Wang, Q. G. Shao, X. Li, L. X. Yuan, X. L. Hu, W. X. Zhang and Y. H. Huang, *Adv. Mater.*, 2012, **24**, 2047.

47 G. Xu, B. Ding, P. Nie, L. Shen, J. Wang and X. Zhang, in *Chem. Eur. J.*, WILEY-VCH Verlag, 2013, vol. 19, pp. 12306.

48 E. Raymundo-Pinero, F. Leroux and F. Beguin, *Adv. Mater.*, 2006, **18**, 1877.

49 Z. Lin, Y. Liu, Y. Yao, O. J. Hildreth, Z. Li, K. Moon and C.-p. Wong, *J. Phys. Chem. C*, 2011, **115**, 7120.

50 D. Hulicova-Jurcakova, M. Kodama, S. Shiraishi, H. Hatori, Z. H. Zhu and G. Q. Lu, *Adv. Funct. Mater.*, 2009, **19**, 1800.

51 J. Chmiola, G. Yushin, Y. Gogotsi, C. Portet, P. Simon and P. L. Taberna, *Science*, 2006, **313**, 1760.

52 C. Largeot, C. Portet, J. Chmiola, P. L. Taberna, Y. Gogotsi and P. Simon, *J. Am. Chem. Soc.*, 2008, **130**, 2730.

53 D. Hulicova-Jurcakova, M. Seredych, G. Q. Lu and T. J. Bandosz, *Adv. Funct. Mater.*, 2009, **19**, 438.

54 D.-W. Wang, F. Li, L.-C. Yin, X. Lu, Z.-G. Chen, I. R. Gentle, G. Q. Lu and H.-M. Cheng, *Chem. Eur. J.*, 2012, **18**, 5345.

55 V. Presser, M. Heon and Y. Gogotsi, *Adv. Funct. Mater.*, 2011, **21**, 810; S. Kondrat, C. R. Perez, V. Presser, Y. Gogotsi and A. A. Kornyshev, *Energy Environ. Sci.*, 2012, **5**, 6474.

56 H. Wang, Z. Li, J. K. Tak, C. M. B. Holt, X. Tan, Z. Xu, B. S. Amirkhiz, D. Harfield, A. Anyia, T. Stephenson and D. Mitlin, *Carbon*, 2013, **57**, 317.

57 W. Xing, S. Z. Qiao, R. G. Ding, F. Li, G. Q. Lu, Z. F. Yan and H. M. Cheng, *Carbon*, 2006, **44**, 216.